PAPER • OPEN ACCESS

First attempt to quantify W7-X island divertor plasma by local experiment-model comparison

To cite this article: Y. Feng *et al* 2021 *Nucl. Fusion* **61** 106018

OPEN ACCESS
IOP Publishing | International Atomic Energy Agency Nuclear Fusion

Nucl. Fusion **61** (2021) 106018 (9pp) https://doi.org/10.1088/1741-4326/ac2025

First attempt to quantify W7-X island divertor plasma by local experiment-model comparison

Y. Feng[1,*], Y. Gao[1], T. Kremeyer[1], D. Gradic[1], L. Rudischhauser[1], G. Fuchert[1], S. Bozhenkov[1], M. Endler[1], M. Jakubowski[1], R. Koenig[1], M. Krychowiak[1], E. Pasch[1], K.C. Hammond[2] and W7-X Team[a]

[1] Max-Planck-Institut für Plasmaphysik, Greifswald, Germany
[2] Princeton Plasma Physics Laboratory, Princeton, NJ, United States of America

E-mail: feng@ipp.mpg.de

Received 31 May 2021, revised 15 July 2021
Accepted for publication 23 August 2021
Published 9 September 2021

Abstract

As a complement to our recent work [1], which focused on understanding the basic detachment physics and general experimental and numerical trends observed in the W7-X island divertor, this paper compares EMC3-Eirene simulation results with different local diagnostics, including IR cameras, Langmuir probes, H_α-cameras, and Thomson scattering. The main purposes are to (1) justify the simulation setup in the previous work, (2) identify the application limitations of the current EMC3-Eirene model, (3) verify the consistency of different diagnostics, and (4) isolate the main geometric and physical effects that need to be prioritized in further developing the EMC3-Eirene code and improving diagnostic capabilities. It turns out that the current version of the EMC3-Eirene code (without drifts) is not yet able to quantitatively reproduce all selected local measurements simultaneously under the current experimental conditions (in particular, the existence of error fields). Nevertheless, it can be shown that within a reasonable range of variation in magnetic configuration, cross-field transport, and SOL plasma state in the modeling, a region of overlap between the numerical results and the local measurements can be established. More accurate model-experiment comparisons will require clarification of error fields, implementation of drifts in EMC3, and improvement of diagnostic capabilities.

Keywords: W7X, divertor, EMC3-Eirene

(Some figures may appear in colour only in the online journal)

* Author to whom any correspondence should be addressed.
[a] See Klinger *et al* 2019 (https://doi.org/10.1088/1741-4326/ab03a7) for the W7-X Team.

1. Introduction

The world's largest highly optimized stellarator, W7-X, is equipped with a so-called island divertor for plasma exhaust [2]. The island divertor uses a chain of magnetic islands inherent in magnetic configurations for which the rotational transform profile crosses a low-order resonance at the plasma edge. The island divertor is fully three-dimensional (3D), not only due to the helically varying form of the island cross-section but also because of the discontinuously installed divertor modules and the resulting localized plasma-wall interaction. The three-dimensionality of the edge plasma and plasma-wall interaction of the island divertor presents a challenge for diagnostics which usually have limited plasma coverage and accessibility.

EMC3-Eirene [3, 4] is a fully 3D edge plasma transport code that comprises reduced fluid models for electrons, ions and impurities, and a kinetic description of neutral gas. Although capable of treating the realistic 3D geometry of the island divertor, it is not yet able to self-consistently describe the island divertor plasma due to the lack of a detailed description of cross-field transport. In the current version of the EMC3-Eirene code, cross-field transport is assumed to be anomalous, and the related transport coefficients are code inputs that need to be determined by fitting experimental measurements. Therefore, it is expected that a combination of the code and local diagnostics is able to provide a more complete and quantitative physical picture of the 3D island divertor plasma. In fact, the EMC3-Eirene code has been routinely applied to W7-X to interpret experimental results, covering a variety of physical topics [1, 5–13]. This work is less physics-oriented. Rather, it focuses on matching 3D code results with various local diagnostics on W7-X simultaneously, with the preliminary goal of clarifying in what aspects and to what extent such a matching procedure is feasible and meaningful for a complex 3D device like W7-X, especially given that there are error fields in the magnetic configuration and the current EMC3 code version does not include drifts.

The next section shows the discharge program and the diagnostics to be compared with modeling. In section 3, we present the current EMC3 model and introduce the transport coefficients that need to be determined experimentally, and then briefly describe how the simulations are set up and conducted. The comparison results are presented in section 4, where challenges and potential physical and technical issues are also discussed. A short summary is given in section 5.

2. Experiment and diagnostics chosen for comparison

The discharge shown in figure 1 (extracted from figure 2 in [1]) was chosen in our previous work as an example for studying the basic physics behind detachment of the W7-X island divertor [1]. There, we focused on general trends without paying much attention to local plasma parameters, and the magnetic configuration and cross-field transport coefficients were chosen and varied without attempting justification. The work in this paper fills this gap by comparing EMC3-Eirene simulations with different local diagnostics. A detailed illustration of

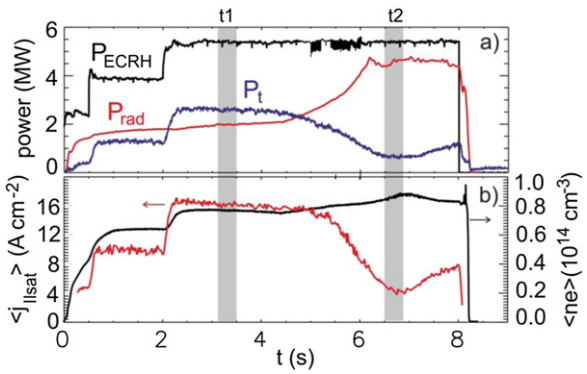

Figure 1. A typical discharge history (#20180814.25) of detachment experiments with the W7-X island divertor. Shown are, from top to bottom, (*a*) ECRH port power P_{ECRH}, the total radiated power P_{rad} provided by a bolometer and the total heat load on targets P_{t} deduced from nine IR-cameras, (*b*) the ion saturation current $j_{\|\mathrm{sat}}$ averaged over all available Langmuir probes (LPs) on the targets and line-averaged density. The two vertical shaded bands indicate two time windows selected for modelling-experiment comparison in this paper.

the discharge history can be found in [1]. Here, we give a brief description of the basic behavior of the most relevant plasma parameters.

It is a hydrogen discharge heated by gyrotrons at the second electron-cyclotron resonance, using the so-called standard divertor configuration (SDC) based on the *iota* $= n/m = 5/5$ island chain. The island control coils are not used here. Using a finite island coil current to increase the island size would cause the strike-line to move further away from the target LPs, which are already displaced from the strike-line of the 'original' SDC island (see later). In this work, the target probes are an important particle diagnostic to be compared with modeling.

The transition to detachment occurs at $t \sim 5.3$ s, at which time the total radiated power P_{rad} measured by the bolometer [14] slightly exceeds 3 MW (figure 1(*a*)), corresponding to a radiation fraction of $f_{\mathrm{rad}} = P_{\mathrm{rad}}/P_{\mathrm{ECRH}}$ (P_{ECRH} = ECRH port power ∼5.5 MW) ∼0.55. The detachment transition is reflected (and defined here) by the abrupt drop in the particle flux on the targets detected by the target LPs [15]. Most of the code-diagnostic comparisons will be performed in the two time windows highlighted in figure 1. In the first time window, the plasma is in an attached state where f_{rad} is about 40%, while in the second time window the plasma is 'deeply' detached, in which $f_{\mathrm{rad}} > 80\%$ and both target particle flux and heat load have a minimum. The heat load is deduced from IR-cameras [16].

The most relevant plasma parameters for determining cross-field transport coefficients are the heat and particle flux distribution on the target, the electron density and temperature profile across the edge magnetic island. For these reasons, the following diagnostics are chosen: (1) two LP arrays, respectively mounted on the two top/bottom symmetric horizontal target plates within one field period (see figure 2), (2) nine IR cameras monitoring nine of the ten divertor modules, with the exception being the lower divertor module instrumented with LPs, (3) an H_α-camera viewing the top divertor module

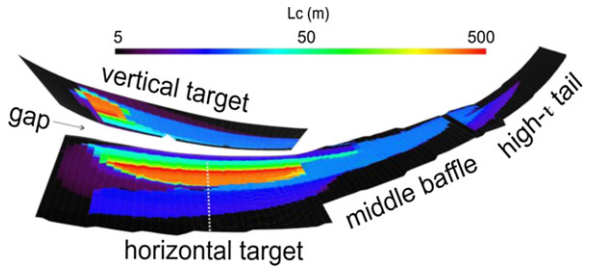

Figure 2. Footprints of flux tubes with different connection lengths on the targets. The dashed white line indicates the location of a target probe array toroidally centred in the footprint of the island tube on the horizontal target. Reproduced from [1]. © EURATOM 2021. CC BY 3.0.

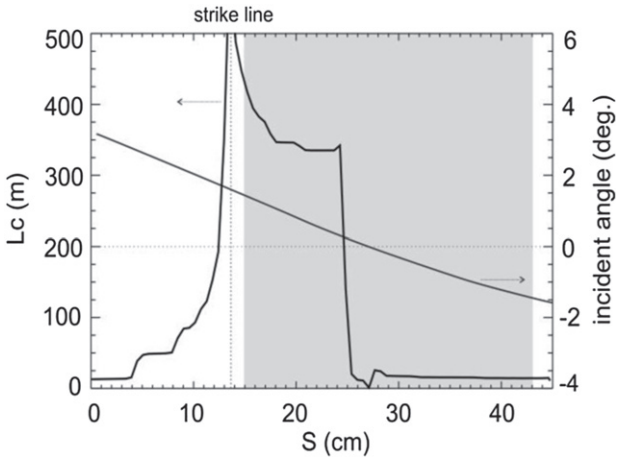

Figure 3. Distributions of connection length and incident angle along the target probe array (figure 2). S on the horizontal axis is the relative distance to the divertor gap. The LP array covers the S-range from 15 cm to 43 cm (shaded region).

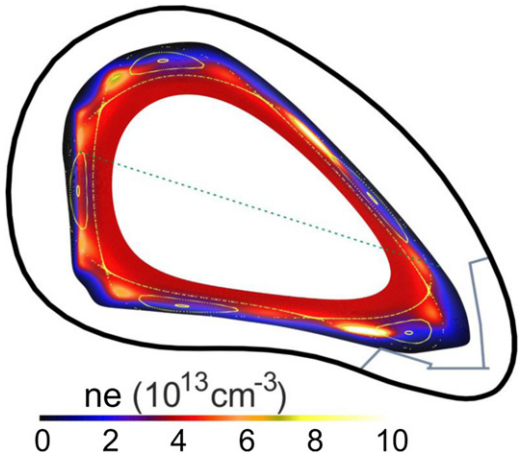

Figure 4. Measurement range of TS at $\phi = \sim 27$ degree (green dashed line). The calculated ne-contour serves only for demonstrating the complexity of plasma distribution expected for the island divertor. Edge magnetic islands are shown by Poincare plots.

equipped with a target probe array, and (4) Thomson scattering (TS) at a toroidal location outside the divertor modules.

The target LPs and the H_α-camera are both important diagnostic instruments for assessing the recycling process. The former directly measure the particle flux onto the target—one of the primary downstream divertor plasma parameters. Unfortunately, these probes have an incomplete coverage of the particle deposition profile (see figure 3). The H_α-camera has a full coverage of the target surface, but interpreting the correlation between the line-integrated H_α-photon flux and the local particle flux on the target is not straightforward, especially under detached conditions. In this regard, the two diagnostics play a complementary role in assessing the particle deposition profile. Unfortunately, the lower target equipped with a LP array is not under H_α-monitoring. Thus, the comparison with simulation results will be made only at the toroidal location of the upper target probe array, with the aim of checking consistency between the two particle diagnostics. Figure 3 displays the connection length and the incident angle along the target probe array, starting from the divertor gap. The strike-line (indicated by the vertical dotted line in figure 3) is about 13–14 cm away from the divertor gap. The incident angle changes sign at $S \sim 26$ cm, which means that plasma flowing onto the left and right sides of the zero incident angle position have opposite parallel velocities.

The laser beam of the TS system passes through a plasma cross-section that is toroidally outside the divertor regions—figure 4(a)). The TS is primarily designed for measuring the core plasma profiles, with only a few channels devoted to the edge magnetic islands. The ne-contour plot in figure 4 is only intended to illustrate the complexity of plasma distribution expected for the island divertor. Quantitative comparison with TS will be given later.

3. The EMC3 model, code inputs and computation setup

The EMC3 code [3] is based on a reduced fluid model consisting of a set of time-independent fluid equations for the mass, momentum and energy of electrons and ions (hydrogen isotopes), which read as

$$\vec{\nabla}\cdot(n_{\rm i}V_{\rm i\|}\vec{b} - D\vec{b}_\perp\vec{b}_\perp\cdot\vec{\nabla}n_{\rm i}) = S_{\rm p} \tag{1}$$

$$\vec{\nabla}\cdot(m_{\rm i}n_{\rm i}V_{\rm i\|}\vec{b} - n_\|\vec{b}\vec{b}\cdot\vec{\nabla}V_{\rm i\|} - D\vec{b}_\perp\vec{b}_\perp\cdot\vec{\nabla}m_{\rm i}n_{\rm i}V_{\rm i\|}) = -\vec{b}\cdot\vec{\nabla}p + S_{\rm m} \tag{2}$$

$$\vec{\nabla}\cdot\left(\frac{5}{2}n_{\rm e}T_{\rm e}V_{\rm i\|}\vec{b} - \kappa_{\rm e}\vec{b}\vec{b}\cdot\vec{\nabla}T_{\rm e} - \frac{5}{2}T_{\rm e}D\vec{b}_\perp\vec{b}_\perp\cdot\vec{\nabla}n_{\rm e} - \chi_{\rm e}n_{\rm e}\vec{b}_\perp\vec{b}_\perp\cdot\vec{\nabla}T_{\rm e}\right) = k(T_{\rm e}-T_{\rm i}) + S_{\rm ee} \tag{3}$$

$$\vec{\nabla}\cdot\left(\frac{5}{2}n_{\rm i}T_{\rm i}V_{\rm i\|}\vec{b} - \kappa_{\rm i}\vec{b}\vec{b}\cdot\vec{\nabla}T_{\rm i} - \frac{5}{2}T_{\rm e}D\vec{b}_\perp\vec{b}_\perp\cdot\vec{\nabla}n_{\rm i} - \chi_{\rm i}n_{\rm i}\vec{b}_\perp\vec{b}_\perp\cdot\vec{\nabla}T_{\rm i}\right) = k(T_{\rm e}-T_{\rm i}) + S_{\rm ei}, \tag{4}$$

where $\boldsymbol{b}$ is the unit vector of the B-field line and $\boldsymbol{b}_\perp\boldsymbol{b}_\perp = \boldsymbol{I} - \boldsymbol{bb}$, with $\mathbf{I}$ being a unit tensor, $\kappa_{\rm e}$ and $\kappa_{\rm i}$ are the Spitzer heat conductivities for electrons and ions, $\eta_\|$ is the parallel viscosity, $m_{\rm i}$

is the ion mass, k is the energy exchange coefficient between electrons and ions, and p is the total plasma thermal pressure of electrons and ions. V_{iII}, n_i, n_e, T_i, T_e are, respectively, the parallel ion streaming velocity, the ion and electron density, and the ion and electron temperature. S_p, S_m, S_{ee} and S_{ei} are the particle, momentum and energy sources due to plasma-neutral interaction. In addition, S_{ee} includes also the energy loss from impurity radiation. All parallel transport processes are classical, while the perpendicular transport processes are assumed to be anomalous with the diffusivity D and the electron and ion thermal conductivities χ_e and χ_i being free input parameters. All cross-field transport coefficients need to be determined by comparisons with experimental measurements—the topic addressed in this paper. There is no solid theory behind the diffusion ansatz for cross-field transport. Clarifying whether, how well, and under what conditions the island divertor plasma in W7-X will meet the diffusion approach would be a long-term project. This work is just the beginning and starts with spatially constant D, χ_e and χ_i, although the code is technically capable of handling non-uniform transport coefficients [17].

The EMC3 code includes a simplified impurity transport that is also based on a fluid approach [18]. Continuity equations for each ionization stage include a classical convection and an anomalous diffusion process parallel and perpendicular to the magnetic field, respectively. Here, the parallel streaming velocity of impurities is determined by a balance among parallel classical forces, while the cross-field diffusivity is assumed to be the same as for the background ions. In this paper, intrinsic carbon is taken as the only impurity species. Carbon transport is not a topic of this work, but its radiation is considered, which enters the electron heat transport channel through S_{ee}—equation (3).

The first difficulty encountered in a model-experiment comparison of local plasma parameters is the lack of precise knowledge of the actual magnetic configuration due to the existence of error fields [19, 20], the elastic deformation of the non-planar coils under electromagnetic forces, and finite-beta effects. Clarification of the uncertainties in magnetic configuration is already a huge topic that is beyond the scope of this paper. Instead, two slightly different configurations are employed to check sensitivity. The two configurations are shown in figure 5. The green configuration is the original SDC, while the red one is created by having a 360 A current in the planar coils, which leads to an inward shift of the 5/5-resonance with respect to the plasma center and moves the strike-line away from the divertor gap. Both are ideal vacuum fields. For the discharge investigated, the volume-average beta is less than 1%, and the resulting beta-effects on the configuration are expected to be smaller than the variation between the two configurations.

A diffusivity of $D = 0.5$ m^2 s^{-1} is assumed for both hydrogen and carbon. The electron and ion thermal conductivities χ_e and χ_i, are set equal and varied between 0.75 m^2 s^{-1} and 1.5 m^2 s^{-1}. A combination with the configuration variation yields three simulation series, as listed in table 1. Further details of the simulation setup and a more comprehensive description of how the simulations are performed are given in [1].

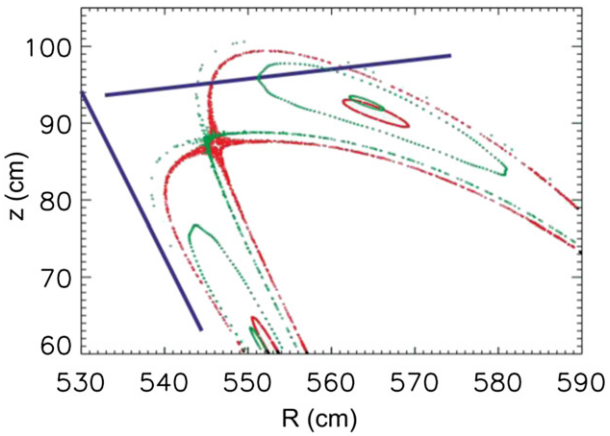

Figure 5. Two configurations are used in the studies to cover uncertainties in the actual configuration. The red one is generated by having a 360 A current (negatively signed in machine operation) in the planar coils to move the island radially inward, while the green one is the standard configuration for which this additional current is set to zero. Reproduced from [1].

Table 1. Computation setup of three simulation series (derived from [1]).

Aeries	Configuration	P_{SOL} (MW)	D (m^2 s^{-1})	$\chi_e = \chi_i$ (m^2 s^{-1})
S1	Original SDC	5	0.5	1.5
S2	Original SDC	5	0.5	0.75
S3	Inward shifted	5	0.5	0.75

4. Comparison results

We start with the IR-cameras. Figure 6 displays the heat flux distributions deduced from the nine IR-cameras within the two time windows highlighted by $t1$ and $t2$ in figure 1, respectively. They are W7-X-symmetrically (fivefold periodicity + stellarator-symmetry) mapped onto the position of the upper target probe array. In the attached case (figure 6(a), the nine dotted profiles differ not only in width, but also in magnitude and peak location, to which neither the periodicity condition nor the stellarator-symmetry condition applies. Note that both conditions are presupposed in the modeling. It is not yet clear how to decode the complex information hidden in the nine IR-profiles. Error fields and drifts are the most likely contributors to the diverse heat flux distributions, and interactions between these two effects may also play a role. Due to the perfect symmetry in the magnetic configuration assumed in the simulations and the absence of drifts in the 3D code, each simulation series results in a single heat load profile (solid curves in figure 6(a)). Under these circumstances, a more suitable method for meaningful comparison between the 3D code and the IR results has not been developed beyond what is simply done in figure 6. Nevertheless, figure 6(a) shows that the blue curve from S3, in which the island chain is slightly

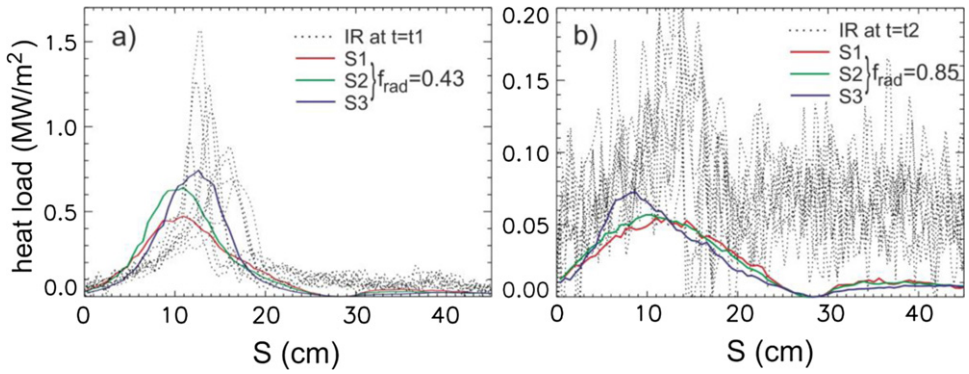

Figure 6. Heat deposition profiles deduced from nine IR-cameras (dotted) in comparison with those resulting from the three simulation series (solid) at (*a*) attachment and (*b*) detachment.

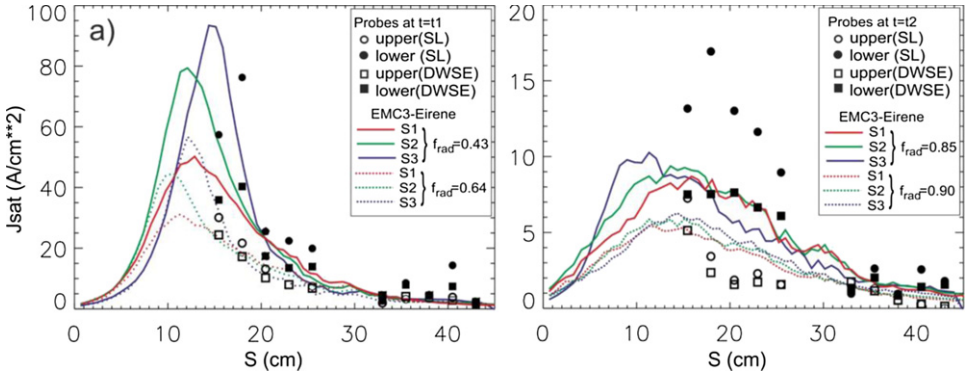

Figure 7. Parallel ion saturation currents from the upper (open symbols) and lower (filled) probe array evaluated based on a simple Langmuir (SL) model (circles) and the so called DWSE model (squares), and calculated parallel particle fluxes from different simulation series (different colors) at (*a*) attachment and (*b*) detachment, in each case, two different f_{rad}-points (solid vs dotted) are taken, considering the uncertainty in the actual radiation intensity. Reproduced from [1].

moved inwards and the perpendicular heat conductivities are both reduced by a factor of two, overlaps more with the group of IR-profiles. The comparison even suggests that one should move the boundary magnetic islands further inward and further reduce the cross-field thermal conductivities, which, however, as will be shown latter, is not supported by the other diagnostics.

At detachment (figure 6(*b*)), there are no noticeable differences among the nine IR-curves. However, in this case, the heat flux on the targets is reduced to a level that is comparable to, or even lower than, the ∼0.15 MW m^{-2} resolution of the IR-cameras [16]. Therefore, it seems to be less meaningful to discuss the IR-results for the detached case. The EMC3-Eirene code shows that the resulting heat flux profiles are insensitive to the variation in magnetic configuration and cross-field heat conductivity undertaken in the simulations. Photon contributions are not taken into account in calculating the heat deposition in the 3D code. A rough estimate by assuming a line radiation source helically along the X-point gives a number that is similar to the IR-curve 'offset' (see figure 6(*b*)), provided that the IR-results there are not pure noise. In fact, this symmetrization tendency of thermal load across different divertor modules toward high radiation levels is a general experimental observation in W7-X [5, 21, 22].

The target LPs directly measure the particle flux on the targets. However, evaluating the LP data is not a straightforward process, even for the ion saturation current. Depending on the degree of physical complexity considered, different evaluation methods exist in the literature, ranging from a simple Langmuir (SL) model to more comprehensive ones, one of which is, for example, the so-called double probe Weinlich–Carlson sheath expansion (DWSE) model (see e.g. [15] and the references therein). The ion saturation currents evaluated with the SL and DWSE models are both shown in figure 7, distinguished by circular and square symbols, (a) at attachment and (b) at detachment. Also shown in figure 7(*a*)) are the simulation results from all three simulation series taken at $f_{rad} = 0.43$ or 0.64, respectively, considering the uncertainty in the actual radiation strength. The numerical results at detachment are depicted in figure 7(*b*) for $f_{rad} = 0.85$ and 0.9, respectively. These comparisons do not aim for perfect agreement between the code and the target probes, but rather outline the range of uncertainties in the modeling and the measurement.

The lower probes measure higher ion saturation currents than the upper ones, and this up/down asymmetry appears to be enhanced at detachment. The lower divertor module equipped

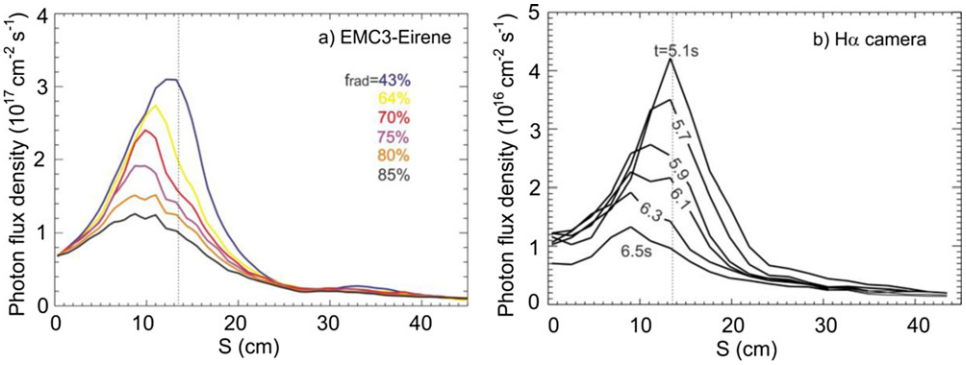

Figure 8. Evolution of H_α-emission profile at the upper target probe location during detachment—EMC3 synthetic from S3 (left) virus H_α-camera.

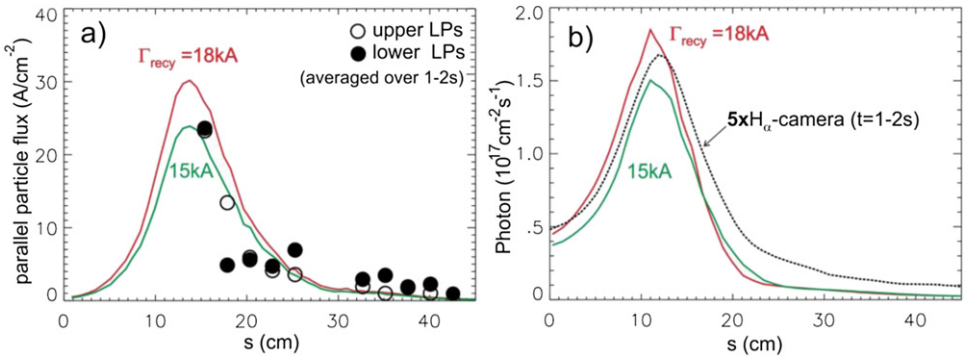

Figure 9. (*a*) Two dedicated EMC3 simulations (continuous lines) for #20181010.10 are aligned with target probe measurements (circles). There is no significant asymmetry in the parallel ion saturation current (from the DWSE model) between the upper and lower target probe array. The two calculations are carried out to verify sensitivity; (*b*) the resulting synthetic H_a-emission profiles (solid curves) along the target probe array in comparison with that from the H_α-camera viewing the upper target array. Note that the measured H_α-photon flux density shown here is multiplied by a factor of 5.

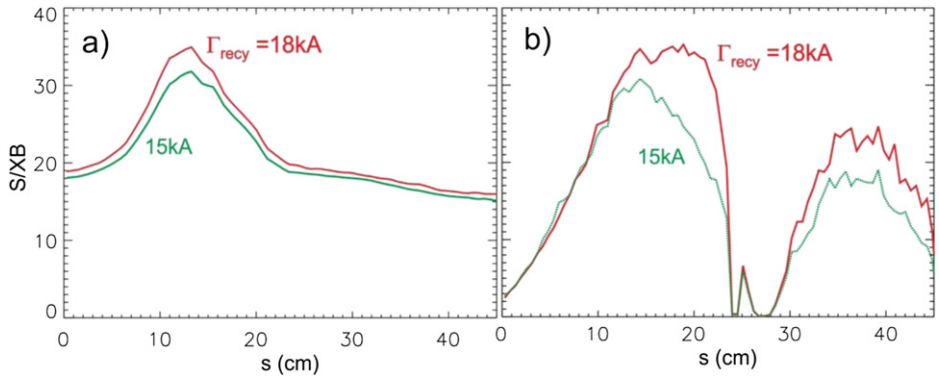

Figure 10. *S/XB* values from two different evaluations: (*a*) the ratio between hydrogen ionization and H_α-emission, which are both integrated along the lines of sight of the H_α-camera viewing the upper target probe array, (*b*) the local particle flux density on the upper target array is normalized to the line-integrated H_α-emission. The differences in *S/XB* between (*a*) and (*b*) are associated with neutral transport.

with target probes is not under IR monitoring, so a possible up/down asymmetry in heat flux between the two divertor modules cannot be excluded—an issue that needs further clarification.

Moreover, the positioning of the target probes does not allow a reasonable assessment of the entire particle deposition profile and the associated anomalous transport coefficients. To solve this problem, we need the help of H_α-cameras. For this purpose, an H_α-synthetic diagnostic has been created in the 3D code. The evolution of the H_α-photon profile during detachment detected by the H_α-camera is depicted in figure 8(*b*), in comparison with the synthetic H_α-emission profiles shown in figure 8(*a*). The profiles are evaluated at the toroidal location of the upper target array. We see that the measured and

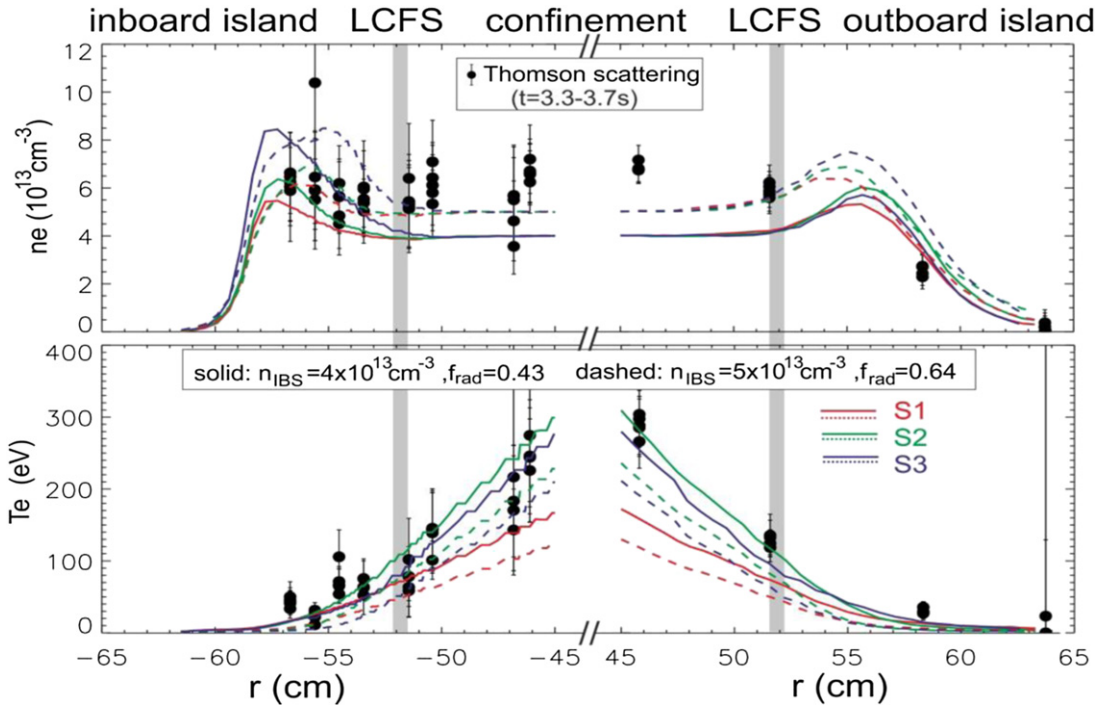

Figure 11. Electron density (top row) and temperature (bottom) profiles from TS (filled circles) and from EMC3-Eirene (curves) at attachment for all three simulation series under two different boundary conditions: (1) $n_{\mathrm{IBS}} = 4 \times 10^{13}$ cm^{-3} with $f_{\mathrm{rad}} = 0.43$ (solid curves), and (2) $n_{\mathrm{IBS}} = 5 \times 10^{13}$ cm^{-3} with $f_{\mathrm{rad}} = 0.64$ (dashed). The TS data along the laser beam (figure 4) are mapped to the grid surfaces labelled by r determined by cylindrically approximating the volume enclosed by each grid surface. Positive and negative sign of r indicates the outboard and inboard side, respectively.

synthetic profiles agree well in shape, peak location, width and dynamics during detachment. However, they differ significantly in magnitude. The predicted H_α-photon flux densities are a factor of about 8–10 higher than those measured by the H_α-camera. This large discrepancy is due in part to the fact that fewer particles reach the upper target area around the probes than the lower target, as shown by the different particle fluxes between the upper and lower target probe array—figure 7. Note that this up/down asymmetry cannot be captured by the EMC3-Eirene code. Subtracting this up/down asymmetry effect, the remaining discrepancies are still factors in the range of 4 to 5.

This issue has recently been re-examined for another discharge (20181010.10) with a lower heating power (4 MW) and at a lower radiation level (∼1 MW). In this discharge, no significant asymmetries in the ion saturation current are observed between the upper and lower target probe arrays, as shown in figure 9. Dedicated EMC3-Eirene simulations use the ion saturation profile measured by the target probes as input. Two calculations with different recycling fluxes are carried out to verify sensitivity. The resulting H_α-emission distributions along the probe array are displayed in figure 9(*b*), compared with that provided by the H_α-camera. The measured and calculated profiles match in shape, but not in absolute magnitude. Note that the measured H_α-photon flux density shown figure 9(*b*) is multiplied by a factor of five—a similar factor as found for #20180814.25. The H_α-photon emission is related to the hydrogen ionization process by a so-called *S*/*XB* value, which describes the ratio between hydrogen ionization and H_α-photon emission. Under the plasma conditions addressed in this paper, the H_α-emission is mainly contributed by hydrogen atoms, including those reflected from target surfaces or produced during molecular dissociation processes. For a given background plasma, the local *S*/*XB* value can be readily found in the atomic database. However, the H_α-camera integrates the local H_α-photon emissivity along the lines of sight. Therefore, an 'effective' *S*/*XB* ratio may be more practical than a local ratio to make the H_α-signal more useful. Depending on which particle quantities we want to associate the line-integrated H_α-signal with, there is no unique definition of an effective *S*/*XB* ratio. Figure 10 shows the effective *S*/*XB* ratios evaluated using two different methods; (a) both local ionization rate and H_α-photon emissivity are integrated along the lines of sight of the H_α-camera viewing the upper target probe array, and (b) the local particle flux density on the upper target array is divided by the line-integrated H_α-emission. The *S*/*XB* values provided by the two methods will be closer to each other as the neutral mean free path length becomes shorter. In other words, the different *S*/*XB* values from the two methods reflect neutral transport effects. We are particularly interested in the two probes closest to the strike-line (figure 9(*a*)) because of their highest ion saturation currents. At these positions, the two evaluation methods yield a similar *S*/*XB* value of about 30, which varies slightly between the two simulations and well lies within the theoretically expected range.

In short, the 3D code cannot quantitatively reproduce the two different particle-relevant diagnostics at the same time. Possible causes are being investigated.

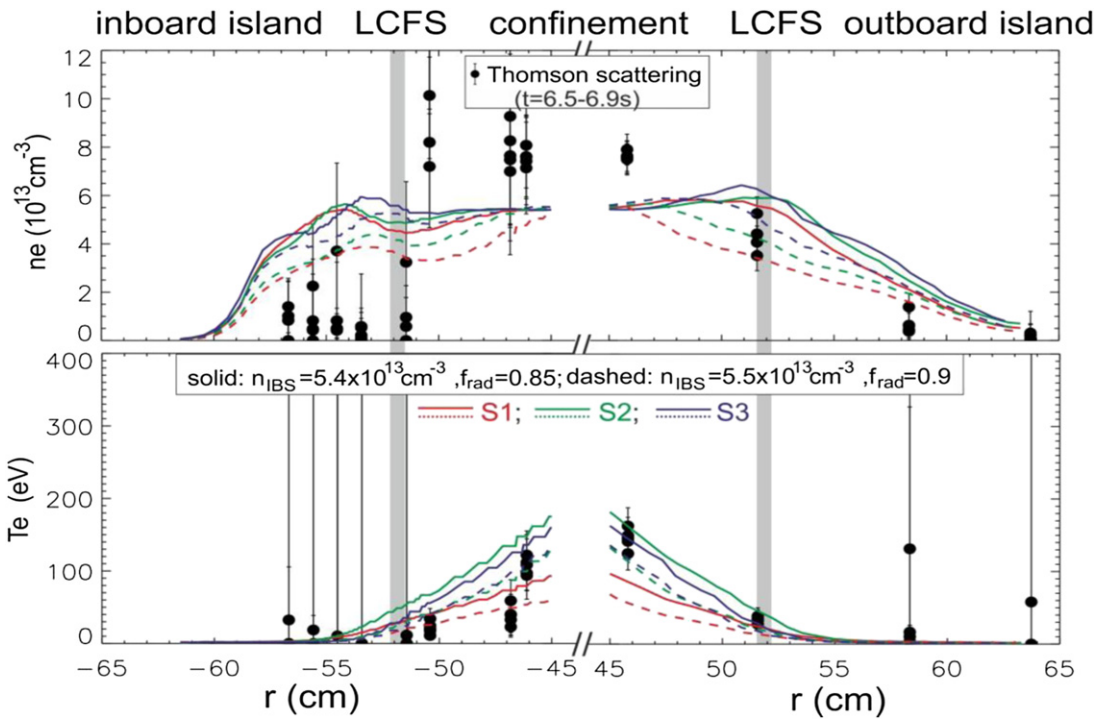

Figure 12. Same as figure 11, but for detachment under two simulation boundary conditions of (1) $n_{\mathrm{IBS}} = 5.4 \times 10^{13}$ cm^{-3} with $f_{\mathrm{rad}} = 0.85$ (solid curves), and (2) $n_{\mathrm{IBS}} = 5.5 \times 10^{13}$ cm^{-3} with $f_{\mathrm{rad}} = 0.9$ (dashed), respectively.

So far, we have focused on the downstream plasma parameters. Now, we turn our attention to upstream parameters and compare the electron density and temperature profiles between the EMC3-Eirene code and the TS. As already demonstrated in figure 4, the calculated island divertor plasma exhibits a complex pattern with fine structures. In the following, we show to what extent the numerical results agree or disagree with the local TS data. To facilitate direct comparison, the TS data along the laser beam is mapped to the radial grid coordinates defined by cylindrically approximating the volume enclosed by each radial grid surface. This approach is meaningful because the radial grid surfaces follow the basic shape of the magnetic flux surfaces formed by the 3D coils [1]. The comparison results for the attached case ($t1$) are displayed in figure 11. The laser beam passes through the edge magnetic islands two times - on the outboard (positive r) and the inboard side (negative r). The TS data in the confinement region outside the simulation domain are omitted. The current TS system is not a diagnostic optimized for the edge island plasma, which is reflected by the incomplete plasma coverage on the inboard side and the insufficient channel resolution on the outboard side. The two groups of simulations depicted in figure 11 are the same as those shown in figure 7(a), thus allowing a more complete view of the quality of the downstream and upstream matches. Within the range of uncertainties in both modeling and measurement, the simulation results roughly agree with the TS data. Better agreement would require fine-tuning and re-combining the code input parameters.

Figure 12 shows the comparison results for the detached case. In this case, the electron temperatures in the edge magnetic islands are too low to be resolved by the TS. The two outermost TS channels in operation for T_{e} are located inside the confinement region, but still near the LCFS (see the lower row of figure 12). T_{e} near the LCFS is an important upstream parameter for assessing the island divertor transport [1], and therefore the TS is a very useful diagnostic for the island divertor. As for the density profiles, the calculated curves, especially the dashed ones at 90% radiation, coincide with the TS data only on the outboard side. On the inboard side, qualitative discrepancies between the calculated and measured densities are found. Since the current TS system is not optimized for the island plasma, especially with low temperatures and densities, these mismatches need to be verified in the next experimental campaign with improved diagnostic capabilities.

5. Summary

EMC3-Eirene simulations have been compared with various local diagnostics (IR-cameras, LPs, H_{α}-cameras, TS) under different SOL plasma conditions ranging from attachment to detachment, as a complement to previous work on understanding detachment of the W7-X island divertor [1]. It has been found that the 3D code in its current state is not yet able to quantitatively reproduce all selected local diagnostics at the same time. Here, drifts and error fields that are missing in the modeling are considered to the biggest obstacles. Nevertheless, it has been shown that within a reasonable range of variation in magnetic configuration, cross-field transport, and SOL plasma state in the modeling, a region of overlap between the numerical results and the local measurements can be

established. Most of the discrepancies are within an understandable range, but there are some exceptions. For example, (1) under attached conditions, the predicted heat flux profiles are almost twice as wide as those deduced from the IR-cameras and there exists a relative displacement in peak location between the calculated and measured heat load profiles. Better agreement with the IR-profiles would be expected by moving the island further inward and reducing the anomalous heat conductivities, which would, however, cause the EMC3-Eirene results to differ from the H_α-camera and TS measurements. In short, with the spatially constant anomalous transport coefficients assumed in the modeling, it is difficult to fit all three measurements. (2) There is a factor of 4–5 difference in absolute H_α-emission flux between the H_α-cameras and the EMC3-Eirene code, or more precisely, between the photon flux captured by the H_α-cameras and that expected from the target probes. (3) At detachment, the calculated density profiles do not match those of the inboard edge Thomson channels, which needs to be clarified in the next experimental campaign with improved diagnostic capabilities. It seems that a detached island plasma poses a challenge to the current TS system and therefore needs its own dedicated TS system.

More accurate model-experiment comparisons will require clarification of error fields, implementation of drifts in EMC3, and improvement of diagnostic capabilities.

Acknowledgments

This work has been carried out within the framework of the EUROfusion Consortium and has received funding from the Euratom research and training programme 2014–2018 and 2019–2020 under Grant Agreement No. 633053. The views and opinions expressed herein do not necessarily reflect those of the European Commission.

ORCID iDs

Y. Gao https://orcid.org/0000-0001-8576-0970
T. Kremeyer https://orcid.org/0000-0002-6383-944X
S. Bozhenkov https://orcid.org/0000-0003-4289-3532
M. Endler https://orcid.org/0000-0003-2314-8393
M. Jakubowski https://orcid.org/0000-0002-6557-3497
K.C. Hammond https://orcid.org/0000-0002-1104-4434

References

[1] Feng Y. *et al* 2021 *Nucl. Fusion* **61** 086012
[2] Sunn Pedersen T. *et al* 2019 *Nucl. Fusion* **59** 096014
[3] Feng Y., Sardei F., Kisslinger J., Grigull P., McCormick K. and Reiter D. 2004 *Contrib. Plasma Phys.* **44** 57
[4] Reiter D., Baelmans M. and Börner P. 2005 *Fusion Sci. Technol.* **47** 172–86
[5] Schmitz O. *et al* 2021 *Nucl. Fusion* **61** 016026
[6] Effenberg F. *et al* 2017 *Nucl. Fusion* **57** 036021
[7] Effenberg F. *et al* 2019 *Nucl. Fusion* **59** 106020
[8] Frerichs H., Effenberg F., Feng Y., Schmitz O., Stephey L., Reiter D. and Börner P. 2017 *Nucl. Fusion* **57** 126022
[9] Winters V.R. *et al* 2021 *Plasma Phys. Control. Fusion* **63** 045016
[10] Cosfeld J., Rack M., Reiter D., Drews P., Feng Y. and Zhang D. 2019 *Nucl. Mater. Energy* **18** 307–11
[11] Stephey L. *et al* 2018 *Phys. Plasmas* **25** 062501
[12] Perseo V., Effenberg F., Gradic D., König R., Ford O.P., Reimold F., Ennis D.A., Schmitz O. and Sunn Pedersen T. 2019 *Nucl. Fusion* **59** 124003
[13] Gao Y. *et al* 2019 *Nucl. Fusion* **59** 106015
[14] Zhang D. *et al* 2010 *Rev. Sci. Instrum.* **81** 10E134
[15] Rudischhauser L. *et al* 2020 *Rev. Sci. Instrum.* **91**
[16] Jakubowski M. *et al* 2018 *Rev. Sci. Instrum.* **89** 10E116
[17] Feng Y. *et al* 2014 *Contrib. Plasma Phys.* **54** 426–31
[18] Feng Y., Lunt T., Sardei F. and Zha X. 2013 *Comput. Phys. Commun.* **184** 1555
[19] Lazerson S.A. *et al* 2018 *Plasma Phys. Control. Fusion* **60** 124002
[20] Bozhenkov S.A., Otte M., Biedermann C., Jakubowski M., Lazerson S.A., Sunn Pedersen T. and Wolf R.C. 2019 *Nucl. Fusion* **59** 026004
[21] Zhang D. *et al* 2019 *Phys. Rev. Lett.* **123** 025002
[22] Jakubowski M. *et al* 2021 Overview of the results from the divertor experiments at Wendelstein 7-X and their implications for steady state operation *28th IAEA Fusion Energy Conf.* (10–15 May 2021) Contribution ID: 1501